Carbon Trends 13 (2023) 100314

Contents lists available at ScienceDirect

Carbon Trends

journal homepage: www.elsevier.com/locate/cartre

Studies on effect of temperature on carbonization of silk (*Bombyx mori*) and its application as proximity sensor

Shubhanth Jain [a], R.V. Prajwal [b], V. Vedavyas [a], S. Vishwas [b], Govindaraj Achutharao [a,*]

[a] Solid State and Structural Chemistry Unit, Indian Institute of Science, Bengaluru, India
[b] Centre for Nano Science and Engineering, Indian Institute of Science, Bengaluru, India

ARTICLE INFO

Keywords:
Silk fibroins
β-Sheet
Carbonization
Graphitization
XPS
XAES
D-parameter
Proximity sensors

ABSTRACT

Silk, a pyroprotein with its unique micro-structural features comprises of soft amorphous α regions containing compact β-sheet crystals resulting in its potent characteristics. Annealing in inert atmosphere causes carbonization followed by graphitization of these stable β-sheet-rich silk fibroins (SFs). Here we carry out systematic studies of annealed silk fibroin (*Bombyx mori*) in the temperature range of 200-1200 °C by various analytical techniques. Herein the structural changes in SFs at different annealing temperature have been discussed using Raman, FTIR, XPS, XAES, SEM, XRD characterization techniques. Notably XPS and XAES studies were executed to examine the influence of sp^2/sp^3 ratio and the presence of hetero-atom on D-parameter value in silk β-sheet material on gradual increase in annealing temperature. The mechanical properties of SFs were measured using UTM. The application of carbonized silk fibroins (CSF) as a proximity sensor is also investigated and proposed as a probable active material.

1. Introduction

The accelerated development of flexible electronics has been observed due to a surge of demand in the market leading to the emergence of diverse flexible devices like sensors and actuators, cells, displays, electronic skins, integrated micro-systems, along with the wide-ranging inclusion of application fields, involving energy and information. Numerous studies have shown carbon precursors as potential materials for the state-of-the-art technologies [1–3]. Silk is one of the predominant natural fibers with distinguished mechanical characteristics of high strength, stiffness, and toughness. It represents an exclusive and crucial class of structural proteins in nature, providing a wide range of native functions, and has long been used as an excellent material for textile manufacturing, cosmetics, and in biomedical and biotechnological fields as drug release, biosensors, tissue regeneration, cell adhesion and growth, and as a capable precursor material for the preparation of medical equipment due to its bio-compatible nature [4–14]. Silk and its composites are being extensively explored as active materials, as well as substrates for the active material in the sensor fields [15–21].

Mulberry Silk is a common form of silk making up to 90% of the global silk production. *Bombyx mori* worms on consuming Mulberry leaves produce the mulberry silk. These are natural protein fibers produced by arthropods and is obtained from cocoon (a protective covering for larvae of silk worm) or spider web, with alanine (ala) and glycine (gly) as main constituents. The predominant elements of silk fibroin derived from *B. mori* are glycine (Gly) at 43%, followed by alanine (Ala) at 30%, and serine (Ser) at 12% in its amino acid composition. Poly-(Gly-Ala) and poly-Ala domains are the primary sequence of amino acid repeat units present in silk fiber [22–27]. Intra/inter chain hydrogen bonds of these two high concentration polypeptide domains design a unique β-sheet secondary structural conformations. A hydrogen atom for gly and a methyl group for ala form short side chains with the repeat units leading to tight stacks of β-sheet crystallites with a rectangular coordinate system [25,28–30].

The cocoon is mainly made up of 70-80% hydrophobic silk fibroins (SFs) and 20-30% of hydrophilic sericin with trace amounts of wax (0.4-0.8%) and natural color (0.2%). Sericin is present as an enclosure over the SFs. SFs comprise of soft amorphous α-helical domains containing compact β-sheet crystals aligned within. Silk protein, with β-sheet conformation as the most stable secondary structure is affiliated with compelling characteristics, especially its unparalleled mechanical properties [31–33]. Due to its biodegradable and bio-compatible nature,

* Corresponding author.
E-mail address: govindaraj@iisc.ac.in (G. Achutharao).

https://doi.org/10.1016/j.cartre.2023.100314
Received 5 August 2023; Received in revised form 29 October 2023; Accepted 20 November 2023
Available online 24 November 2023

many research groups are changing the properties of silk by compositing the fibers either by feeding the silkworms or chemical processing of silk fibers with materials for applications in wearable sensors, synthetic tissue or low-cost triboelectric nanogenerator sprays [7,34–36]. Tian et al., have demonstrated the possibility of mass production of these modified silk fibers by developing breeding schemes [37].

The pyrolytic behavior (heating in an inert atmosphere not leading to melt or evaporate out, rather transforming into a carbonaceous solid) of silk proteins without presence of any aromatic backbones or cross-linked structures implies that the protein molecules were restructured to form unsaturated aromatic structures. *B. mori* SFs serve as a prime example of fibrous proteins that possess crystalline β-sheets. Cho et al., have shown β structure transformation via pseudo-graphitic crystalline layers to form a highly ordered graphitic structures at higher temperatures i.e., the chemical transformation of β-sheet structures of *B. mori* silk into poly-hexagonal carbon structures, pyroproteins, through heating (Supplementary Information (SI) Figure - 1) [30].

Full apprehension of the graphitization process of carbon materials derived from organic precursors continues to pose a significant challenge. It is widely acknowledged that multiple stages are implicated in the transformation to nanoscale unsaturated aromatic constituents, which are generated through the thermal decomposition of the primary silk structure into well-organized carbon graphitic frameworks. These steps include reactions taking place concurrently like elimination of hetero-atoms, condensation and dehydration on heating to higher temperatures. Likewise, silk experiences alterations in the parallel arrangement and stacking of poly-hexagonal carbon units when subjected to annealing, facilitating the formation of extended, highly ordered graphitic structures that are not present at lower temperatures (SI Figure - 1) [30,38–40].

The heat-treated SFs are analyzed using various characterization techniques like X-ray Photoelectron Spectroscopy (XPS), XAES, Raman spectroscopy and Fourier Transform Infrared (FTIR) spectroscopy. In this article we report the transformation of SF to higher order form through heat treatment complimentary to the existing understanding via XPS and XAES. The dependence of the D-parameter (obtained by XAES) on the transformation of poly-hexagonal carbon structure below and above the onset of thermal carbonization (~250-350 °C) were studied in detail. The poly-hexagonal carbon structures are derived from the transformation of β-sheet crystallites, while preserving their parallel alignment.

A proximity sensor is a device capable of detecting the approach of an object towards it without any physical contact. Various types of proximity sensors are available with different mechanisms and fabrications for diverse applications [41–48]. We have explored the proximity sensing properties of carbonized silk fibroins (CSFs) annealed at 800 °C, 1000 °C and 1200 °C through preliminary measurements.

2. Experimental procedure

2.1. Materials

Silk was obtained from silk merchants and considered as raw silk (RS) for further treatment, Graphite powder (< 50 μm) and Dimethyl Sulfoxide (DMSO) from Merck KGaA, Polyimide substrate from Lab Supplies Pvt. Ltd. Bangalore and Parylene for coating from Specialty Coating Systems.

2.2. Degumming of silk

Raw silk (RS) was degummed using the hydrothermal treatment, a chemical-less route with only water as a solvent. Briefly, the degumming was carried out in a 80 mL Teflon-lined autoclave by taking 1.2 g of silk fiber and 57 mL water at a constant temperature of 120 °C for 3 hours to obtain optimally degummed sample. It was then rinsed with water and dried at 60 °C yielding 0.9 g of degummed sample. A degumming ratio (D_r) of ~25% was observed for the sample. The effect of temperature and silk:water ratio taken on degumming is tabulated in Supplementary Information (SI Table-1).

2.3. Annealing of silk

The degummed SF were annealed to various temperatures (200, 300, 400, 600, 800, 1000 and 1200 °C) in a tube furnace in an inert gas (nitrogen) atmosphere. In a typical procedure, ultra-high purity (UHP) nitrogen gas is passed through a mass flow controller (make: Line-Tech, South Korea), further purified by passing it through a heated (250 °C) copper tower and connected to a quartz tube. The quartz tube is then positioned within a tube furnace. The degummed SFs are carefully positioned within the quartz tube at the center of the furnace. The samples are subsequently heated to the desired temperatures while maintaining a consistent flow rate of purified nitrogen (50 standard cm^3/min). The temperature is increased gradually at a ramp rate of 3.5 °C/min, and the samples are allowed to soak at the target temperature for a duration of 30 minutes. These heated samples were named as s200, s300 and so on to reflect the temperature of annealing. The samples annealed to temperatures above 200 °C are collectively referred to as CSF. Colour change in the silk fiber to brown was observed at 200 °C and subsequently to black at 300 °C under nitrogen atmosphere (SI Figure-2). Similarly, the degummed SF were also annealed under rotary vacuum (10^{-3} Torr) to 200 °C at similar rate and duration, which was named as v200.

2.4. Material characterization

Powder X-Ray Diffraction (PXRD) pattern of the samples was obtained using a Cu-K_α source with wavelength 1.54 Å in Empyrean, Malvern Panalytical instrument. The scan was conducted within the 2θ range of 5-80°, with a step size of 0.01 and a scan rate of 150 seconds/step. Thermogravimetric Analysis (TGA) data was obtained from Mettler Toledo AG - TGA/SDTA851e fitted with TSO800GC1 gas controller in Nitrogen flow of 10 mL/min at a ramp rate of 2 K/min up to a temperature of 600 °C. Surface area measurements were carried out using BELSORP-max ll, manufactured by MicrotracBEL Corp. using constant volume gas adsorption method + AFSM™. The Degassing was done for 12 h at 100 °C.

X-Ray Photoelectron Spectroscopy (XPS) was carried out using Thermo Scientific K-ALPHA instrument with an Al-K_α source ($h\nu$ = 1486.6 eV). The spectra were gathered using the constant energy mode in the analyzer, employing a pass energy of 50 eV. The scan step size was set at 0.10 eV, and a spot size of 400 μm was used. Spectroscopic data were processed by the CasaXPS v2.2.84 software, using a peak-fitting routine with symmetrical/asymmetrical Gaussian–Lorentzian functions. The Shirley background was used for the photoelectron spectra. Infrared Spectrum of all samples were obtained from PerkinElmer LR-64912C Fourier Transform Infrared (FT-IR) spectrometer with an universal Attenuated Total Reflection (ATR) attachment. The spectra were collected over the range 400-4000 cm^{-1} by co-adding 64 scans. The Raman spectroscopy analysis was done in the Horiba LabRAM instrument using a 532 nm laser at 1% power and grating used was 600 mm^{-1}. Spectra were collected from 10 accumulations of 20 seconds each. Scanning Electron Microscope (SEM) imaging was carried out using Ultra55 FE-SEM Karl Zeiss instrument. The images were captured using the secondary electron detector mode, utilizing a low EHT of 3 kV. For assessment of the strength of heat treated fibers, a single strand of SF having a length of 50 mm was placed carefully on a rectangular cardboard using double sided tape (SI Figure-7). The gauge length of the sample was 30 mm. Cardboard was placed in a micro-UTM MultiTest 10-i machine. The sides of cardboard were cut at the dotted line shown in SI Figure-7, prior to measurements to make sure tensile loading was applied only on the sample. A load cell of 25 N

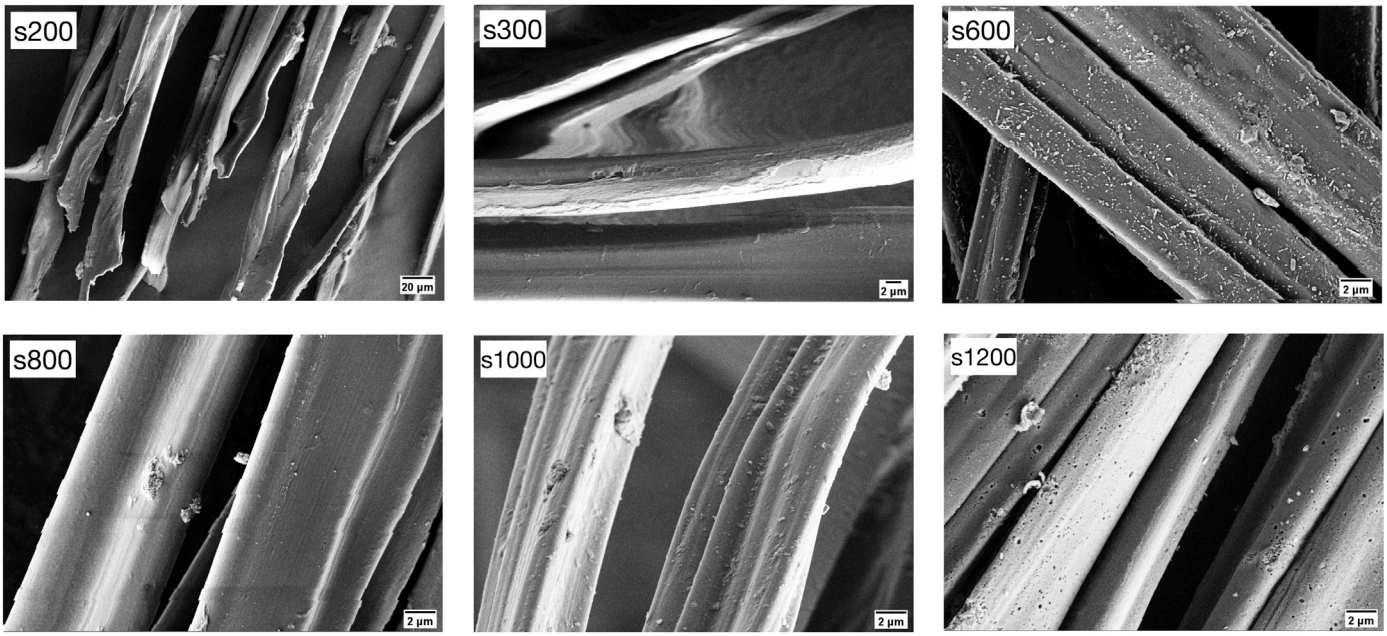

Fig. 1. SEM images of s200, s300, s600, s800, s1000 and s1200.

was taken for the experiments. All tests were conducted at a rate of 2 mm/min under ambient conditions of 22 °C and ~45% humidity. A set of 5 trials was done for each sample. To check the resistance of a single CSF strand, the ends of the strand were connected tautly to copper tapes kept at a distance of 5 mm using a conducting silver paste on a glass substrate (SI Figure-8). The resistances of CSF of different temperatures were recorded using a multimeter and tabulated as Table 2. The selected samples (s800, s1000, s1200) for proximity sensor assessment were ground and dispersed in DMSO at a concentration of 10 mg/mL via bath sonication and drop-casted onto a polyimide substrate placed on a glass plate. Silver wires were attached to the film using silver paste and connected to a GWINSTEK GDM-8261A Dual Display Digital MultiMeter (DMM). The sample was given a coating of parylene using SCS Labcoter 3 Parylene Deposition System 2010 (thickness - 500 nm) to prevent environmental effects like humidity and reaction with gases. The fabricated sensor cartoon diagram is shown in SI Figure-8.

3. Results and discussion

The XRD pattern of the samples heated at 800, 1000 and 1200 °C (SI Figure-4) indicate a broad Bragg's reflection at 25° and 45°; the 25° reflection denoting the graphitization peak (002). However, these Bragg reflections increased markedly in the silk protein samples with higher annealing temperatures, indicating deformation of the β-sheet structure and increasing sp^2 characteristic, which arise due to the thermal degradation of the silk protein occurring at temperatures exceeding 300 °C.

The TGA plot (SI Figure-5) shows weight loss beginning at 200 °C, while significant loss occurs at ~300 °C due to carbonization where the conversion of β-sheet to carbon hexagonal structure occurs accompanied by release of gases [40], which can also be corroborated from the blackening of the samples (SI Figure-3). The yield obtained on annealing silk in furnace can be matched with the loss seen in the TGA plot.

The surface area measurements indicated that as the annealing temperature increased, there was an enhancement in the area, which is tabulated in Supplementary Information (SI Table-3). A significant surge in surface area was observed between s800 and s1000, which could be attributed to the evolution of heteroatoms within the structure SI Figure-1.

SEM images of samples (Fig. 1) shows shrinkage of silk fibers with increase in temperature with a significant reduction in size at s300 due to onset of carbonization. Pore evolution on the surface of fiber can be seen at 600 °C with their number and size increasing thereafter.

The structure of proteins is widely determined by the three distinguishable types of vibration peaks associated to the amide groups, namely, amide I, amide II and amide III [49–51]. The amide I band arise at ~1660 cm^{-1} (α form) and ~1630 cm^{-1} (β form) due to C=O stretching, while the amide II band is attributed to N-H bending, accounting for the broad peak spanning from 1560 to 1516 cm^{-1}. The amide III band corresponds to stretching vibrations of C-N bonds in aliphatic amines, specifically assigned to the 1190-1250 cm^{-1} range. Ambrose et al., have shown that the α and β configurations of polypeptides can be recognized by the C=O stretching mode (amide I band), which is at ~1660 cm^{-1} for the α form and ~1630 cm^{-1} for the β form [52]. This shift exhibits similarities to the observed transition from the soluble native state to the insoluble denatured state [52]. The presence of the α peak at 1698 cm^{-1} and the β peak at 1620 cm^{-1} can be observed in the FTIR spectra of CSF, as depicted in Fig. 2(A), extending until s300. Also, the absorption of amide I band of β-sheet is greater than that of α form indicating probable higher percentage of β-sheet conformation [53,54]. In s400, these amide I peaks have disappeared due to its transformation to poly-hexagonal carbon structures (SI Figure - 1). The amide II and amide III bands are also seen to disappear in s400 indicating onset of carbonization. Two intense broad peaks are seen to develop at ~1560 cm^{-1} and between 1000 and 1150 cm^{-1} starting from s600, corresponding to conjugated cyclic C=C stretching vibration and aryl or vinyl C-O stretching vibration respectively, which confirms the increase in sp^2/sp^3 ratio seen in XAES analysis. Another peak of interest is the one at ~1700 cm^{-1}, which could also be assigned to carboxylic C=O stretching, which is seen to decompose after 300 °C. The frequencies at which these vibrations occur is affected by the conformation of polypeptides in the silk fiber [55].

The Raman spectra of the annealed SF samples ranging from 200 to 1200 °C are illustrated in Fig. 2(B). In Raman spectroscopy, the G band is directly associated with sp^2 bonds, while the D band arises from the presence of sp^2 microdomains that result from bond angle disorder induced by sp^3 hybridizations. Spectra of SF and CSF samples show various Raman bands indicative of bonds and structure of the polymer. At 300 °C, the spectrum shows the evolution of G and D bands which are indicative of sp^2 and sp^3 carbons respectively. The annealed samples above 300 °C showed the disappearance of many bands due

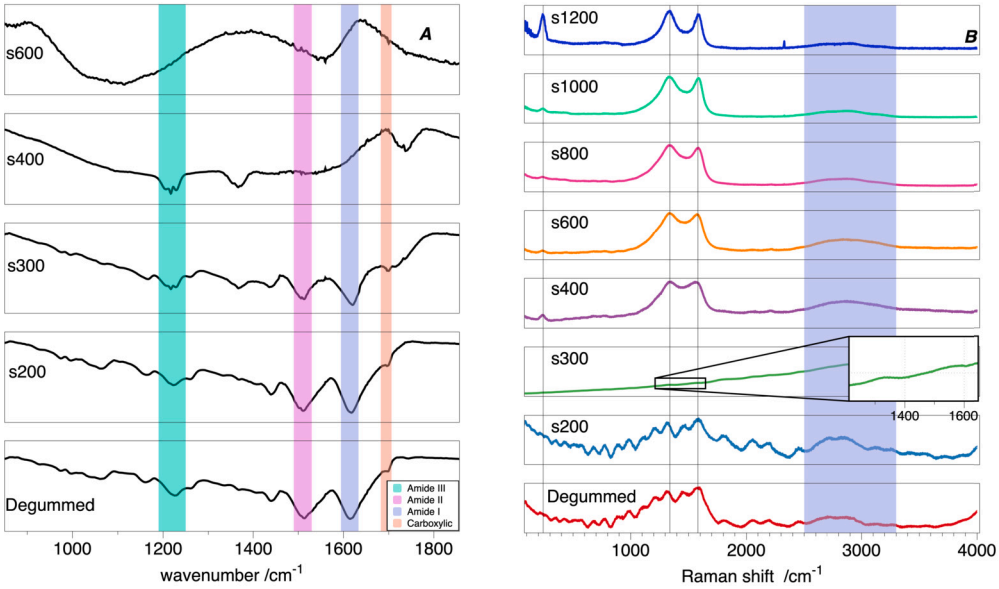

Fig. 2. (A) Comparison of FTIR Spectra of CSFs showing changes in amide bands. (B) Comparison of Raman Spectra of CSFs showing development of G and D bands at 300 °C and their narrowing with increase in annealing temperature.

to carbonization except for D, G (which occur at ~1,350 and ~1,580 cm^{-1}) and 2D band (~2690 cm^{-1}) corresponding to stable β-sheet structure, characterized by a three-dimensional-ordered hexagonal carbon arrangement, that was preserved with minor alterations. Another way to describe this process is the conversion of stable silk protein, which is rich in β-sheets, into a pseudographitic pyroprotein. The band at 240 cm^{-1} may probably correspond to transverse acoustic of phonon dispersion of graphitic layer [56,57]. In the spectrum, the G and D bands become narrowed and more pronounced with annealing temperature, due to the increased amount and ordering of graphitic phase [58–62].

XPS analysis was carried out on degummed silk and CSFs (200-1200 °C) as seen in Fig. 3. Chemical transition around 300 °C, and the formation of higher aromatic structures in s400 is noticed as confirmed by the FTIR spectra Fig. 2(A).

In the N_{1s} spectrum of s200, three separate peaks can be observed. One of these peaks is centered at 399.78 eV, while the other is located at 399.08 eV. These peaks correspond to the O=C-N and C-N bonds, respectively, and exhibit similarity to the spectra of degummed silk proteins [63]. The third peak at 401.5 eV corresponding to H-bridges or hydrogen bridge structures (H-BS) [64].

At s300, three peaks are detected, with one centered at 399.38 eV, corresponding to an amide bond and another centered around 400.1 eV, indicating the presence of nitrogen-bonded (pyridonic) compounds, with the final peak at ~401.6 attributed to convolution of nitrogen-bonded oxide of N compounds [30] and H-BS.

This is indicative of the presence of pyridonic (SI Figure-6(A)) functional group formed from the broken chains and peptide bonds. The s400 spectrum demonstrates the development of a peak at 400.98 eV, which corresponds to the binding energy associated with a specific type of nitrogen species in graphite (referred to as graphitic N), along with oxide of N (possibly pyridinic oxide SI Figure-6(D)) at around 402-404 eV. Graphitic nitrogen is bonded to three carbon atoms, also known as substituted nitrogen or quaternary nitrogen. Pyridinic-N species (structural skeleton of graphitic and pyridinic N in SI Figure-6(B)(C)) is seen at BE ~398.68 eV along with the decreased pyridonic-N concentration at ~400.05 eV [65]. s600 shows similar deconvolution as s400. s800 shows the complete loss of pyridonic group and a similar trend is followed in s1000. s1200 looses all the other groups with retention of only graphitic N (~400.9 eV).

Carbonization takes place via the release of oxygenated functional groups and later their sulfur and nitrogen equivalents [40]. The loss of oxygen and nitrogen content at around 300-350 °C marks the transition temperature for SFs due to formation of ordered hexagonal carbon structures with heteroatoms. Deconvolution of C_{1s} spectra of degummed and CSF is attempted in Fig. 3(B). With the varied carbon environment resulting from different amino acids present in *B. mori*, SF deconvolution is successfully carried out. The density functional theory (DFT) calculations yielded lower binding energy (BE) values for carbon species with sp^2 hybridization compared to those found in perfect graphite. Additionally, the BE values increased for carbon nanostructures that contained electron-withdrawing groups such as defects (like pentagons and hexagons) and hydrogen [66–69]. The experiments conducted on various carbon nanomaterials revealed a separation value in the binding energy (BE) between C sp^2 and C sp^3, which ranged from 0.6 eV to 1.35 eV [66,70–72]. Diamond-like carbon (DLC) films were reported to have binding energy (BE) values of 0.6 eV [73] and 0.8 eV [70]. Graphene oxide exhibited a BE value of 0.7 eV [74], while graphite had a BE value of 0.9 eV [71,75,76], 1.3 eV for onion-like diamond [77] and 1.35 eV for amorphous carbon [78].

Fixing C-C at ~284.75 eV, C=C at ~284.04 eV, convoluting C-N and C-O at ~286.16 eV, amide carbon O=C-N at ~288.05 eV and terminated O=C-OH at ~288.85 eV, the C_{1s} peaks were fit in 3B [79]. The hydrogen bridge binding energy is assigned at ~289.28 eV [64].

The degummed silk showed C_{1s} spectra with all the above mentioned deconvolutions. Predominance in the C-N, O=C-N and O=C-OH counts were observed in s200 and s300 samples compared to degummed samples. The terminated O=C-OH at ~288.85 eV and H-BS at ~289.28 eV are convoluted to a single peak. The vibrational peaks of the functional groups were also seen in the FTIR spectra (Fig. 2(A)). s400 spectrum showed important changes with decrease in concentrations of all the deconvolutions relative C-C sp^3 component i.e., decrease in the carboxylic and (C-N, C-O) components along with the disappearance of amide group and appearance of asymmetric sp^2 component, which is also confirmed from the FTIR spectrum. These are in agreement with the already existing N_{1s} spectra by Cho et al., where it is mentioned about the disappearance of amide at 350 °C [30]. The asymmetric sp^2 component is an indication of β-sheet structure being converted into thermally stable aromatic structure after the thermal degradation at 350 °C. The evolution of sp^2 is observed in s400 at 284.04 eV. O=C-OH and H-BS peak disappearance has been noticed in s600 along with increased peak area of sp^2 component. A considerable

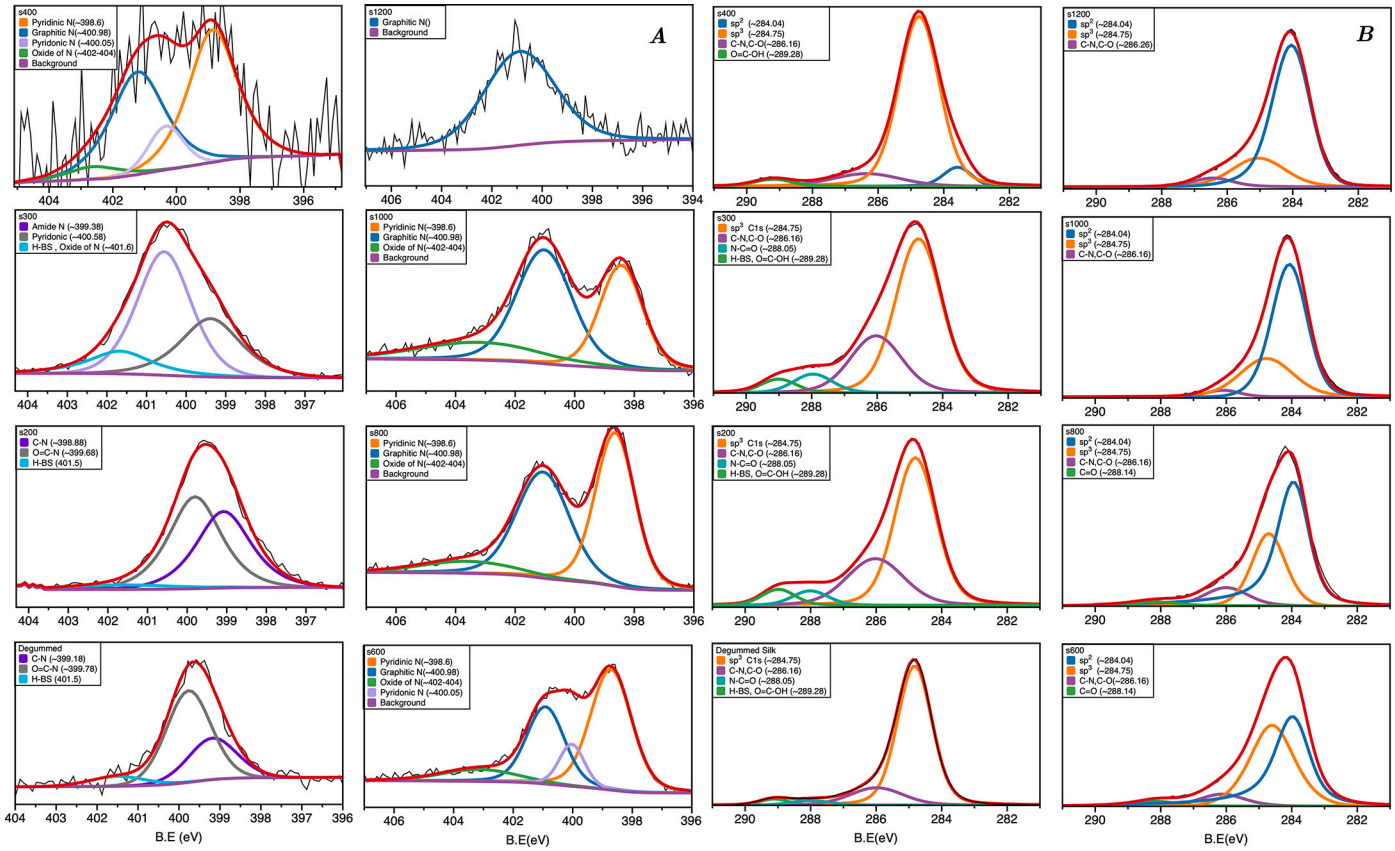

Fig. 3. Deconvoluted XPS spectra for (A) N_{1s} and (B) C_{1s} of annealed and degummed samples according to probable chemical environment.

increase in the sp^2 component in s800, s1000 and s1200 is seen as a result of annealing temperature.

Carbon's electronic spectra consist of two primary excitations: the photoemission line originating from C_{1s} and the Auger line commonly referred to as C KLL. The C KLL line is a combination of C KVV transitions, specifically 1s-2pπ-2pπ and 1s-2pσ-2pπ. This convolution enables the differentiation of various chemical environments and carbon hybridizations [80].

The derivative spectra of carbon samples obtained from X-ray auger electron spectroscopy (XAES) exhibit a distinct fine structure (~265-275 eV) that can be attributed to KVV transitions involving π electrons (Fig. 4(A)). Conversely, variations observed in the 240-260 eV range reflect the influence of many-body correlation effects [81]. The spectrum of C KVV represents a self-convolution of the occupied valence band states, allowing for differentiation between carbon atoms in distinct hybridization states. The morphology of the KLL Auger spectrum observed in carbon nanostructures is indicative of the density of electronic states (DOS) and incorporates the influences of sp^2 (graphite) and/or sp^3 (diamond) hybridization. In the case of hetero-atoms, the spectrum's shape reveals chemical effects specific to those atomic environments. Binding energy of π electrons is less than 5 eV and that of σ electrons is about 8 eV [82–84] given by Equation (1).

$$E_k \approx C_{1s} - V_i - V_j \quad (1)$$

where E_k is Auger electrons' kinetic energies, C_{1s} the binding energy of the carbon 1s level and V_{ij} are valence electrons' binding energies involved in transitions referred to the Fermi level.

Experimental evidence has firmly established that the dominant factor contributing to the intensity of the Auger band in the energy range $E_k > \sim 265$ eV is the presence of π electrons [86]. In a simplified approximation, the elevation of the Auger band beyond approximately 265 eV is attributed to the proportional increase in the concentration of pπ electrons (i.e., sp^2 site concentrations). Previous attempts have been made to determine the sp^2/sp^3 ratio of such structures based on this premise [83,84,87]. Lascovich et al., proposed an evaluation of the C sp^2/sp^3 content based on a parameter D, which represents the energy difference between the maximum and minimum points of the first-derivative C KLL spectrum. It is expected that the relationship between parameter D and C sp^2/sp^3 hybridizations will exhibit linearity, with D values of graphite and diamond serving as reference points. D represents the energy difference between the peak of the positive excursion and the trough of the negative excursion in the first derivative of the C KVV spectra. Using the characteristic C KVV spectral shapes of diamond and graphite as reference benchmarks [88,89], Lascovich et al., estimated the proportion of carbon atoms bonded in the sp^2 configuration in amorphous carbon films [83,84]. Zemek et al., have shown that the parameter D is influenced by the presence of hetero-atom (in carbon nitride system) has high influence and sp^2/sp^3 percentage is not the sole reason for the KLL structure [90]. Their research demonstrated a decrease in the D-parameter as the oxygen percentage on the surfaces increased, suggesting a correlation with the degradation of the carbon network rather than the presence of a distinct phase. Considering the complex bonding arrangements of atoms in the native oxide, the authors concluded that the exact value of the D parameter may exhibit minimal dependence on the hybridization of carbon within the layers. As the probing depth of C KVV electrons is significantly limited, the spectral line shape of C KVV is expected to be influenced by the composition of a near-surface region approximately 3 nm in thickness. The impact of oxygen on the spectral shape of the C KVV line has been previously documented in the literature [83,89,91]. Galuska et al., conducted measurements of C KVV spectra and valence band spectra on graphite surfaces that had undergone oxidation [89]. Comparing to clean graphitic surfaces, narrower line widths were observed in spectra for the oxidized graphite surfaces. Lee et al., have studied systematic sequence of synthetic polymers made up of carbons with varying ratios of

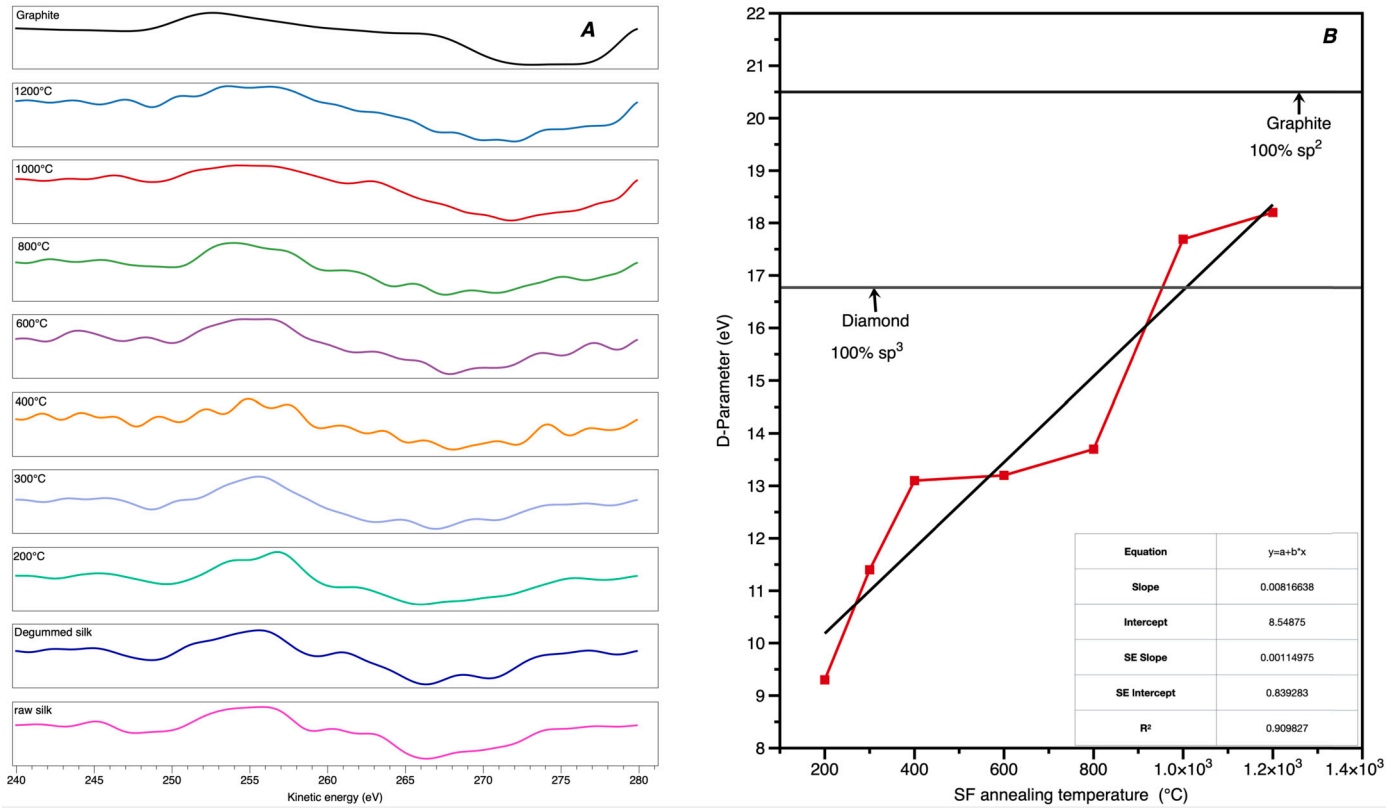

Fig. 4. (A) First-derivative of C KLL Auger spectra of CSFs (s200-s1200). (B) Plot of D-parameter vs temperature showing a linear increase (the value for D-parameter of diamond was obtained from [85]).

sp^2-to-sp^3 hybridization states and linear correlations with D-parameter was proposed [85].

Considering more complicated carbon-based systems like the β sheet structure of silk, we have correlated the annealing temperature (i.e. extent of carbonization) and parameter D. Auger spectra imposed on strong background are discerned by taking first derivative. To differentiate the C KVV spectra, a Savitzky-Golay smoothing technique with a convolution array of 13 points and a 2^{nd} order polynomial was employed [92].

The plot of D-parameter against annealing temperature is given in Fig. 4(B). The D-parameter value of a graphite reference powder showed 20.5 eV. Reference values of graphite and diamond are represented for clarity. An escalation in the D-parameter value with the annealing temperature can be seen in the plot and the values tabulated in Table (SI Table-4). The low linearity may be due to the hetero atoms (O, N) present in the carbon hexagonal structures and their transitions/structural changes/decomposition occurring at different temperatures i.e., amide bond removal, carboxylic decomposition and cyclizations through the temperatures. Cho et al., have shown the existence of carbon hexagonal structure with presence of heteroatoms in annealed samples between s300 to s800 leading to D-parameter value below 16.77 eV (the value of diamond), while the elimination of hetero atoms takes place between s800 to s1000 (SI Figure-1) causing a slight jump in the D-parameter of ~4 eV at that region [30]. With the removal of hetero atoms, the already existing planar carbon hexagonal structure, presence of N in graphitic form (N), and increase in the sp^2 concentration, the D-parameter value enters the diamond-graphite region. It is important to note the constant increase D-parameter value outside the diamond-graphite region as well.

Mechanical properties of silk are seen in the force-displacement curves (Fig. 5) for raw silk, degummed silk, s200 and v200. RS bears the highest load of 0.844±0.012 N. DS can bear a lesser load of 0.568±0.038 N. v200 withstands a load of 0.568±0.021 N close to the strength of DS. The force borne by s200 was 0.315±0.030 N which is less than vacuum annealed sample. A possible explanation for this observation is that vacuum thermal treatment causes a quick rise in temperature, which prevents the silk fibers from undergoing complete reactions compared to the fibers that underwent slow thermal treatment under nitrogen flow. This is also evident in Table 1, where v200 fibers have larger diameter than s200 fibers. It should also be noted that the SFs of v200 were less carbonized than s200 as seen in SI Figure-3. The s200 sample has a darker appearance than the v200 sample. Raw silk has more plastic deformation than degummed silk. From the tensile test the extensibility of vacuum annealed sample is better than the nitrogen treated sample.

The young's modulus, yield stress, ultimate tensile stress and percentage of elongation were calculated [93,94] and tabulated in Table 1. The stiffness of v200 (~15.519±2.92 GPa) and s200 (~13.718±0.86 GPa) were observed to be in a similar range while a difference in percentage elongation was observed. The ultimate strength for the v200 (~566.23±21.8 MPa) is more than the s200 (~335.41±32.84 MPa). As SFs are carbonized to higher temperature, their strength goes on decreasing. Compared to carbonization in nitrogen atmosphere, the samples gave better strength when treated in vacuum. Articles show an increase in the mechanical strength of the mulberry silk, which may be due to treatment of silk at the phase transition temperature of 350 °C for 3 hours before further annealing for complete rearrangement to stable β form [31].

Table 2 gives the resistance of 5 mm of silk threads as described earlier. We are exploring the possibility of using the CSF of 800, 1000 and 1200 °C as a proximity sensor material. To get changes in resistance values, the sensor was connected to a DMM (Digital Multi-Meter) with a viewer software and the readings were plotted. The schematic representation of the set-up used for the measurement is given in SI Figure-9. A constant baseline could not be obtained due to the effect of humidity and other environmental factors on the sensor [41]. The sensor was then

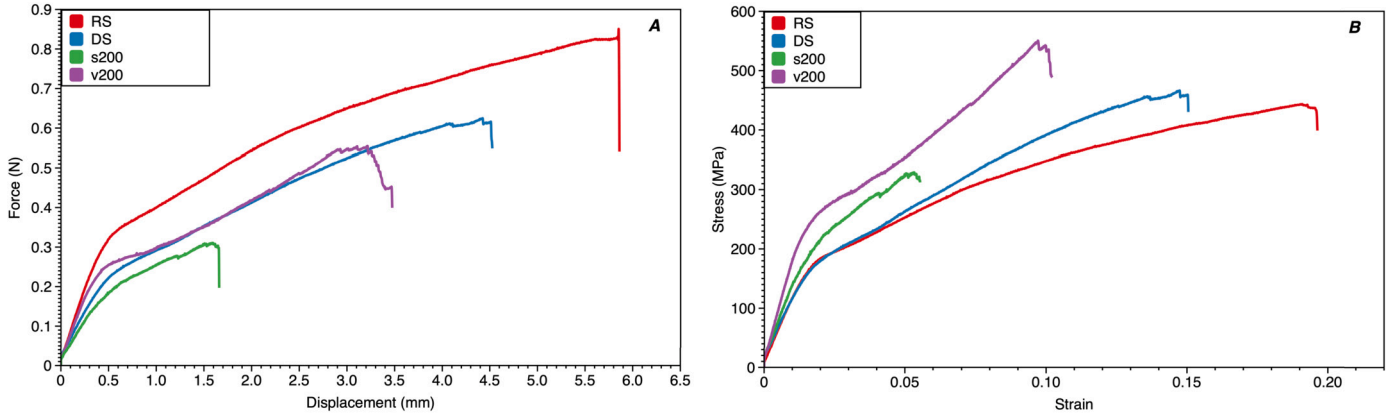

Fig. 5. Plots showing mechanical properties of SFs: (A) stress vs strain curves; (B) force vs displacement curves.

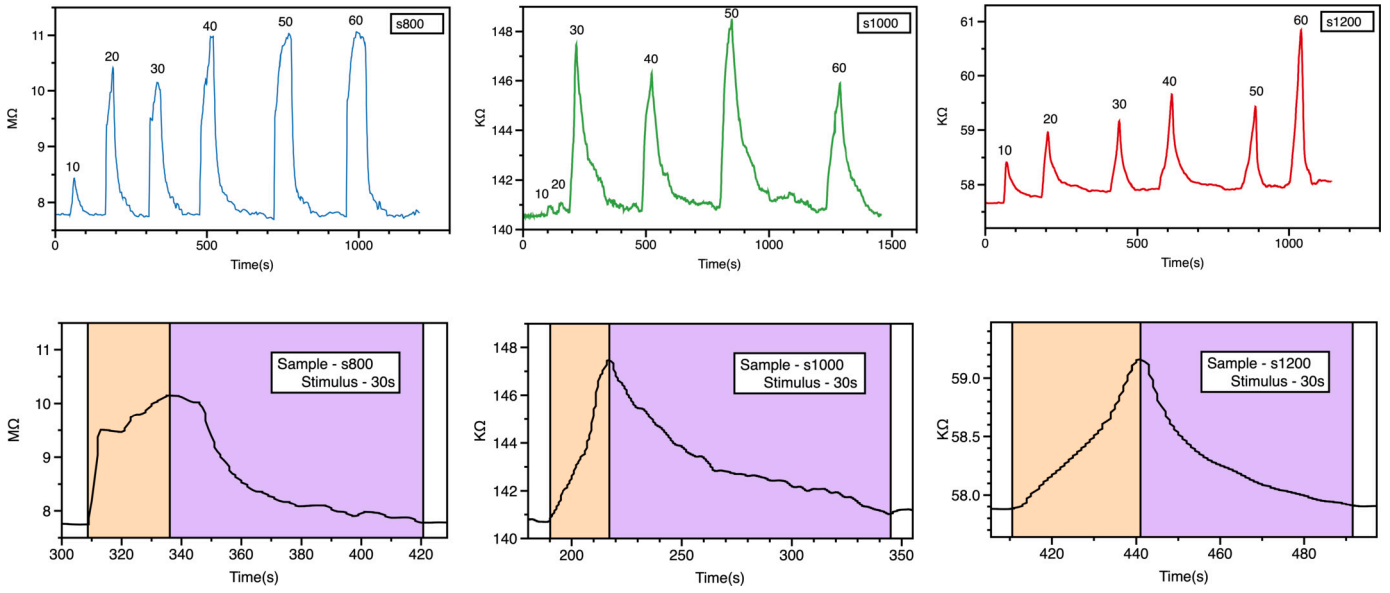

Fig. 6. (Top) Resistance vs time plots showing the performance of s800, s1000 and s1200 as proximity sensor. The values on the peaks refer to the amount of time stimulus was given to the sensor material; (Bottom) response-recovery curves of the samples for 30 s stimulus. The response to stimulus is indicated by the yellow-brown color, while the purple color indicates the recovery time.

Table 1
Mechanical properties of raw silk, degummed silk, s200 and v200 samples.

Sample Name	Diameter (μm)	Force (N)	Elastic Modulus (GPa)	Yield Stress (MPa)	Yield Strain	UTS (MPa)	Elongation %
RS	35.15	0.844±0.01	10.751±0.29	173.804±3.70	0.0182±0.00	434.936±6.50	18.912±0.88
DS	10.66	0.569±0.04	8.653±1.30	142.666±23.15	0.0187±0.00	424.895±28.92	15.527±0.36
s200	8.95	0.315±0.03	13.718±0.86	228.102±23.86	0.0195±0.00	335.411±32.85	4.859±0.56
v200	9.24	0.568±0.02	15.519±2.92	250.814±6.76	0.0189±0.00	566.235±21.82	11.653±1.78

Table 2
Electrical conductivity of SFs annealed at different temperatures.

Temperature (°C)	Resistance (kΩ)
700	2630
800	42.6
900	11.6
1000	7.1
1100	4.26
1200	2.11

coated with parylene and the response of the sensor to static electrons is shown in Fig. 6. Although the sensor showed changes in resistance values at a stimulus distance of around 15-20 mm, the readings were noted at a minimum distance of ~1 mm between the object and sensor to adeptly evaluate the material as an active material in proximity sensors. s1200 has demonstrated the best response and recovery times, along with better consistent response to the stimulus. Further details have been mentioned in SI. High-performance commercial displacement sensors use limited sensing surfaces to notice the targets positioned close to them and have usual sensing ranges between 0.05 and 50 mm. It is important to mention that the sensor structure influence the measurement, and hence optimization the electrodes' parameters to obtain highly sen-

sitive, robust, flexible sensor with highest design priority for a practical application will be carried out in future.

4. Conclusion

Partial graphitization of mulberry silk fibroins was carried out by carbonizing at various temperatures between 300-1200 °C in an inert atmosphere and characterized systematically. The XAES shows the correlation of D-parameter with annealing temperature. From the D-parameter plot, it is observed that presence of hetero-atoms makes the hexagonal carbon sheet less ordered than the diamond reference value. A linearity is seen throughout the temperature range for the silk polymer even outside the diamond-graphite region. Gradual increase in degree of graphitization of the SF (β-sheets) is confirmed with the XAES and XPS studies with increase in temperature. Further, CSFs s800, s1000 and s1200 were used for proximity sensor characteristic studies. It is observed that the silk carbonized at 1200 °C showed good sensitivity to the static electrons on human fingers. The optimal working distance of the sensor was found to be 10-15 mm and the sensor took 25-35 seconds for recovery. With the flexible characteristic of carbonized silk and its sensitivity in electrical resistance to static electron proximity, we propose it as a viable candidate for further sensor studies.

Declaration of competing interest

The authors declare that they have no known competing financial interests or personal relationships that could have appeared to influence the work reported in this paper.

Data availability

Data will be made available on request.

Acknowledgement

We dedicate this article to Prof. C. N. R. Rao, FRS on his 90th birthday.

This research was performed using SSCU Characterization Facility at IISc, Bangalore, supported by DST-FIST, UGC-CAS and IISc-MoE funding initiatives.

We acknowledge support from CeNSE (MNCF) facilities funded by MHRD, MeitY and DST Nano Mission.

We express our utmost and sincere gratitude to Prof. M. M. Nayak, CeNSE, IISc for his assistance in the fabrication of sensor and its measurement.

Appendix A. Supplementary material

Supplementary material related to this article can be found online at https://doi.org/10.1016/j.cartre.2023.100314.

References

[1] Elzbieta Frackowiak, Carbon materials for supercapacitor application, Phys. Chem. Chem. Phys. 9 (15) (2007) 1774–1785, https://doi.org/10.1039/B618139M.
[2] S.R.C. Vivekchand, et al., Graphene-based electrochemical supercapacitors, J. Chem. Sci. 120 (2008) 9–13, https://doi.org/10.1007/s12039-008-0002-7.
[3] Abisola Opeyemi Egbedina, et al., Emerging trends in the application of carbon-based materials: a review, J. Environ. Chem. Eng. 10 (2) (2022), https://doi.org/10.1016/j.jece.2022.107260.
[4] Xiaoping Liang, et al., Stable and biocompatible carbon nanotube ink mediated by silk protein for printed electronics, Adv. Mater. 32 (31) (2020) 2000165, https://doi.org/10.1002/adma.202000165.
[5] Fatemeh Ganjali, et al., Biocompatibility and antimicrobial investigation of agar-tannic acid hydrogel reinforced with silk fibroin and zinc manganese oxide magnetic microparticles, J. Inorg. Organomet. Polym. Mater. 32 (10) (2022) 4057–4069, https://doi.org/10.1007/s10904-022-02410-0.
[6] Chunya Wang, et al., Silk-based advanced materials for soft electronics, Acc. Chem. Res. 52 (10) (2019) 2916–2927, https://doi.org/10.1021/acs.accounts.9b00333.
[7] Jugal Kishore Sahoo, et al., Silk chemistry and biomedical material designs, Nat. Rev. Chem. 7 (5) (Apr. 2023) 302–318, https://doi.org/10.1038/s41570-023-00486-x.
[8] Ke Wang, et al., Preparation of bacterial cellulose/silk fibroin double-network hydrogel with high mechanical strength and biocompatibility for artificial cartilage, Cellulose 27 (2020) 1845–1852, https://doi.org/10.1007/s10570-019-02869-0.
[9] Thang Phan Nguyen, et al., Silk fibroin-based biomaterials for biomedical applications: a review, Polymers 11 (12) (2019), https://doi.org/10.3390/polym11121933.
[10] Shovon Bhattacharjee, et al., Graphene- and nanoparticle-embedded antimicrobial and biocompatible cotton/silk fabrics for protective clothing, ACS Appl. Bio Mater. 4 (8) (2021) 6175–6185, https://doi.org/10.1021/acsabm.1c00508.
[11] Mhd Anas Tomeh, Roja Hadianamrei, Xiubo Zhao, Silk fibroin as a functional biomaterial for drug and gene delivery, Pharmaceutics 11 (10) (2019), https://doi.org/10.3390/pharmaceutics11100494.
[12] Xiang-Long Lin, et al., Mechanical property and biocompatibility of silk fibroin–collagen type II composite membrane, Mater. Sci. Eng., C (ISSN 0928-4931) 105 (2019) 110018, https://doi.org/10.1016/j.msec.2019.110018.
[13] A. Alessandrino, et al., SilkBridge™: a novel biomimetic and biocompatible silk-based nerve conduit, Biomater. Sci. 7 (10) (2019) 4112–4130, https://doi.org/10.1039/C9BM00783K.
[14] Hamid Asadi, et al., Cellulose nanocrystal reinforced silk fibroin coating for enhanced corrosion protection and biocompatibility of Mg-based alloys for orthopedic implant applications, Prog. Org. Coat. (ISSN 0300-9440) 161 (2021) 106525, https://doi.org/10.1016/j.porgcoat.2021.106525.
[15] Shubhanth Jain, et al., Silk and its composites for humidity and gas sensing applications, Front. Chem. 11 (Mar. 2023), https://doi.org/10.3389/fchem.2023.1141259.
[16] Yuxin He, et al., Multifunctional wearable strain/pressure sensor based on conductive carbon nanotubes/silk nonwoven fabric with high durability and low detection limit, Adv. Compos. Hybrid Mater. 5 (3) (2022) 1939–1950, https://doi.org/10.1007/s42114-022-00525-z.
[17] Qianying Chen, et al., Silk-based electrochemical sensor for the detection of glucose in sweat, Biomacromolecules 23 (9) (2022) 3928–3935, https://doi.org/10.1021/acs.biomac.2c00753.
[18] Dan-Liang Wen, et al., Silk fibroin-based wearable all-fiber multifunctional sensor for smart clothing, Adv. Fiber Mater. 4 (4) (2022) 873–884, https://doi.org/10.1007/s42765-022-00150-x.
[19] Dan-Liang Wen, et al., Recent progress in silk fibroin-based flexible electronics, Microsyst. Nanoeng. 7 (1) (2021) 1–25, https://doi.org/10.1038/s41378-021-00261-2.
[20] Zhan Yang, et al., Carbonized silk nanofibers in biodegradable, flexible temperature sensors for extracellular environments, ACS Appl. Mater. Interfaces 14 (16) (2022) 18110–18119, https://doi.org/10.1021/acsami.2c00384.
[21] Ibrahim M. Badawy, et al., Natural silk for energy and sensing applications: a review, Environ. Chem. Lett. 19 (3) (2021) 2141–2155, https://doi.org/10.1007/s10311-020-01161-z.
[22] Xuedong Chen, et al., Combined analysis of silk synthesis and hemolymph amino acid metabolism reveal key roles for glycine in increasing silkworm silk yields, Int. J. Biol. Macromol. 209 (2022) 1760–1770, https://doi.org/10.1016/j.ijbiomac.2022.04.143.
[23] Meghan McGill, Gregory P. Holland, David L. Kaplan, Experimental methods for characterizing the secondary structure and thermal properties of silk proteins, Macromol. Rapid Commun. 40 (1) (2019) 1800390, https://doi.org/10.1002/marc.201800390.
[24] Xiuying Liu, et al., Chemical modification of silk fibroin through serine amino acid residues, Materials 15 (13) (2022), https://doi.org/10.3390/ma15134399.
[25] Cong-Zhao Zhou, et al., Silk fibro structural implications of a remarkable amino acid sequence, Proteins 44 (2) (2001) 119–122, https://doi.org/10.1002/prot.1078.
[26] David Kaplan, Kevin McGrath, Protein-Based Materials, Bioengineering of Materials, Birkhäuser, Boston, MA, ISBN 9780817638481, 1997, https://doi.org/10.1007/978-1-4612-4094-5.
[27] Charu Vepari, David L. Kaplan, Silk as a biomaterial, Prog. Polym. Sci. 32 (8) (2007) 991–1007, https://doi.org/10.1016/j.progpolymsci.2007.05.013.
[28] Yuan Cheng, et al., On the strength of β-sheet crystallites of *Bombyx mori* silk fibroin, J. R. Soc. Interface 11 (96) (2014) 20140305, https://doi.org/10.1098/rsif.2014.0305.
[29] Anja Glišović, et al., Strain dependent structural changes of spider dragline silk, Macromolecules 41 (2) (2008) 390–398, https://doi.org/10.1021/ma070528p.
[30] Se Youn Cho, et al., Carbonization of a stable β-sheet-rich silk protein into a pseudographitic pyroprotein, Nat. Commun. 6 (1) (2015) 1–7, https://doi.org/10.1038/ncomms8145.
[31] Se Youn Cho, et al., Ultra strong pyroprotein fibres with long-range ordering, Nat. Commun. 8 (1) (2017), https://doi.org/10.1038/s41467-017-00132-3.
[32] Shaoyong Chen, et al., Mechanical properties of Bombyx mori silkworm silk fibre and its corresponding silk fibroin filament: a comparative study, Mater. Des. (ISSN 0264-1275) 181 (2019) 108077, https://doi.org/10.1016/j.matdes.2019.108077.
[33] Zhangchuan Peng, et al., Structural and mechanical properties of silk from different instars of Bombyx mori, Biomacromolecules 20 (3) (2019) 1203–1216, https://doi.org/10.1021/acs.biomac.8b01576.

[34] Nuno Ramos, et al., Toward spinning greener advanced silk fibers by feeding silkworms with nanomaterials, ACS Sustain. Chem. Eng. 8 (32) (2020) 11872–11887, https://doi.org/10.1021/acssuschemeng.0c03874.

[35] Anjana Baburaj, Subrata Das, Dye fed silkworms to produce naturally coloured silk cocoons, J. Nat. Fibers 19 (13) (2022) 5651–5662, https://doi.org/10.1080/15440478.2021.1889430.

[36] Julia N. Fountain, et al., Towards non-stick silk: tuning the hydrophobicity of silk fibroin protein, ChemBioChem 23 (22) (2022) e202200429, https://doi.org/10.1002/cbic.202200429.

[37] Yaxi Tian, et al., A novel transgenic silkworm line for mass production of azido-incorporated silk fiber, J. Silk Sci. Technol. Jpn. 30 (2022) 75–85, https://doi.org/10.11417/silk.30.75.

[38] Gwyn Morgan Jenkins, Kiyoshi Kawamura, Polymeric Carbons: Carbon Fibre, Glass and Char, Cambridge University Press, ISBN 9780521206938, 1976, https://www.cambridge.org/us/universitypress/subjects/engineering/materials-science/polymeric-carbons-carbon-fibre-glass-and-char.

[39] M. Beatriz Vázquez-Santos, et al., Comparative XRD, Raman, and TEM study on graphitization of PBO-derived carbon fibers, J. Phys. Chem. C 116 (1) (2012) 257–268, https://doi.org/10.1021/jp2084499.

[40] Agnes Oberlin, Carbonization and graphitization, Carbon 22 (6) (1984) 521–541, https://doi.org/10.1016/0008-6223(84)90086-1.

[41] Yong Ye, et al., A review on applications of capacitive displacement sensing for capacitive proximity sensor, IEEE Access 8 (2020) 45325–45342, https://doi.org/10.1109/ACCESS.2020.2977716.

[42] Takuya Kurihara, et al., A study of proximity sensor circuit focusing on variations in antenna impedance, in: 2022 IEEE 33rd Annual International Symposium on Personal, Indoor and Mobile Radio Communications (PIMRC), 2022, pp. 01–05, https://doi.org/10.1109/PIMRC54779.2022.9977674.

[43] T.N. Satish, et al., Investigation into the development and testing of a simplex capacitance sensor for rotor tip clearance measurement in turbo machinery, Exp. Tech. 42 (6) (2018) 575–592, https://doi.org/10.1007/s40799-018-0281-y.

[44] Mark Woike, Ali Abdul-Aziz, Michelle Clem, Structural health monitoring on turbine engines using microwave blade tip clearance sensors, in: Smart Sensor Phenomena, Technology, Networks, and Systems Integration 2014, in: International Society for Optics and Photonics, vol. 9062, SPIE, 2014, pp. 167–180, https://doi.org/10.1117/12.2044967.

[45] Wayne C. Haase, Zachary S. Haase, High-speed, capacitance-based tip clearance sensing, in: 2013 IEEE Aerospace Conference, IEEE, 2013, pp. 1–8, https://doi.org/10.1109/AERO.2013.6496903.

[46] Walter J. Bowers, Douglas A. Olson, A capacitive probe for measuring the clearance between the piston and the cylinder of a gas piston gauge, Rev. Sci. Instrum. 81 (3) (2010), https://doi.org/10.1063/1.3310092.

[47] K. Khawaja, L. Seneviratne, K. Althoefer, Wheel-tooling gap measurement system for conform™ extrusion machinery based on a capacitive sensor, J. Manuf. Sci. Eng. 127 (2) (2005) 394–401, https://doi.org/10.1115/1.1870004.

[48] Tommaso Addabbo, et al., A clearance measurement system based on on-component multilayer tri-axial capacitive probe, Measurement 124 (2018) 575–581, https://doi.org/10.1016/j.measurement.2018.01.015.

[49] Yan Ji, et al., DFT-calculated IR spectrum amide I, II, and III band contributions of N-methylacetamide fine components, ACS Omega 5 (15) (2020) 8572–8578, https://doi.org/10.1021/acsomega.9b04421.

[50] Jovencio Hilario, Jan Kubelka, Timothy A. Keiderling, Optical spectroscopic investigations of model β-sheet hairpins in aqueous solution, J. Am. Chem. Soc. 125 (25) (2003) 7562–7574, https://doi.org/10.1021/ja030039e.

[51] T.A. Keiderling, Vibrational CD of biopolymers, Nature 322 (6082) (1986) 851–852, https://doi.org/10.1038/322851a0.

[52] Edmund J. Ambrose, et al., Water-soluble silk: an α-protein, Nature 167 (1951) 264–265, https://doi.org/10.1038/167264a0.

[53] Xiao Hu, David Kaplan, Peggy Cebe, Determining beta-sheet crystallinity in fibrous proteins by thermal analysis and infrared spectroscopy, Macromolecules 39 (18) (2006) 6161–6170, https://doi.org/10.1021/ma0610109.

[54] H. Chen, X. Hu, Peggy Cebe, Thermal properties and phase transitions in blends of Nylon-6 with silk fibroin, J. Therm. Anal. Calorim. 93 (1) (2008) 201–206, https://doi.org/10.1007/s10973-007-8885-y.

[55] Lawrence F. Drummy, et al., Thermally induced α-helix to β-sheet transition in regenerated silk fibers and films, Biomacromolecules 6 (6) (2005) 3328–3333, https://doi.org/10.1021/bm0503524.

[56] Michele Lazzeri, et al., Impact of the electron-electron correlation on phonon dispersion: failure of LDA and GGA DFT functionals in graphene and graphite, Phys. Rev. B 78 (2008), https://doi.org/10.1103/PhysRevB.78.081406.

[57] Jiang-Bin Wu, et al., Raman spectroscopy of graphene-based materials and its applications in related devices, Chem. Soc. Rev. 47 (5) (2018) 1822–1873, https://doi.org/10.1039/C6CS00915H.

[58] Libo Deng, et al., Carbon nanofibres produced from electrospun cellulose nanofibres, Carbon 58 (2013) 66–75, https://doi.org/10.1016/j.carbon.2013.02.032.

[59] Yo-Rhin Rhim, et al., Changes in electrical and microstructural properties of microcrystalline cellulose as function of carbonization temperature, Carbon 48 (4) (2010) 1012–1024, https://doi.org/10.1016/j.carbon.2009.11.020.

[60] Andrea C. Ferrari, Denis M. Basko, Raman spectroscopy as a versatile tool for studying the properties of graphene, Nat. Nanotechnol. 8 (4) (2013) 235–246, https://doi.org/10.1038/nnano.2013.46.

[61] Andrea C. Ferrari, et al., Raman spectrum of graphene and graphene layers, Phys. Rev. Lett. 97 (18) (2006), https://doi.org/10.1103/PhysRevLett.97.187401.

[62] Yan Wang, Daniel C. Alsmeyer, Richard L. McCreery, Raman spectroscopy of carbon materials: structural basis of observed spectra, Chem. Mater. 2 (5) (1990) 557–563, https://doi.org/10.1021/cm00011a018.

[63] Li Zhou, et al., X-ray photoelectron spectroscopic and Raman analysis of silk fibroin–Cu (II) films, Biopolymers 82 (2) (2006) 144–151, https://doi.org/10.1002/bip.20472.

[64] Nidhi Aggarwal, et al., Protein nanofibril design via manipulation of hydrogen bonds, Commun. Chem. 4 (1) (2021) 62.

[65] Takahiro Kondo, et al., Observation of Landau levels on nitrogen-doped flat graphite surfaces without external magnetic fields, Sci. Rep. 5 (1) (2015), https://doi.org/10.1038/srep16412.

[66] Ayaka Fujimoto, et al., Origins of sp^3C peaks in C_{1s} X-ray photoelectron spectra of carbon materials, Anal. Chem. 88 (12) (2016) 6110–6114, https://doi.org/10.1021/acs.analchem.6b01327.

[67] Alexei Barinov, et al., Imaging and spectroscopy of multiwalled carbon nanotubes during oxidation: defects and oxygen bonding, Adv. Mater. 21 (19) (2009) 1916–1920, https://doi.org/10.1002/adma.200803003.

[68] Alexei Barinov, et al., Initial stages of oxidation on graphitic surfaces: photoemission study and density functional theory calculations, J. Phys. Chem. C 113 (21) (2009) 9009–9013, https://doi.org/10.1021/jp902051d.

[69] Alexei Barinov, et al., Defect-controlled transport properties of metallic atoms along carbon nanotube surfaces, Phys. Rev. Lett. 99 (4) (2007), https://doi.org/10.1103/PhysRevLett.99.046803.

[70] Yusuke Mizokawa, et al., The C KLL first-derivative X-ray photoelectron spectroscopy spectra as a fingerprint of the carbon state and the characterization of diamondlike carbon films, J. Vac. Sci. Technol., A, Vac. Surf. Films 5 (5) (1987) 2809–2813, https://doi.org/10.1116/1.574312.

[71] Rainer Haerle, et al., sp^2/sp^3 hybridization ratio in amorphous carbon from C $1s$ core-level shifts: X-ray photoelectron spectroscopy and first-principles calculation, Phys. Rev. B 65 (4) (2001), https://doi.org/10.1103/PhysRevB.65.045101.

[72] B. Lesiak, et al., Influence of the preparation conditions of Pd-ZrO_2 and AuPd-ZrO_2 nanoparticle–decorated functionalised MWCNT s: electron spectroscopy study aided with the QUASES, Surf. Interface Anal. 49 (11) (2017) 1124–1134, https://doi.org/10.1002/sia.6290.

[73] J.F. Morar, et al., C 1s excitation studies of diamond (111). I. Surface core levels, Phys. Rev. B 33 (2) (1986) 1340–1345, https://doi.org/10.1103/PhysRevB.33.1340.

[74] L. Stobinski, et al., Graphene oxide and reduced graphene oxide studied by the XRD, TEM and electron spectroscopy methods, J. Electron Spectrosc. Relat. Phenom. 195 (2014) 145–154, https://doi.org/10.1016/j.elspec.2014.07.003.

[75] Stuart T. Jackson, Ralph G. Nuzzo, Determining hybridization differences for amorphous carbon from the XPS C 1s envelope, Appl. Surf. Sci. 90 (2) (1995) 195–203, https://doi.org/10.1016/0169-4332(95)00079-8.

[76] Javier Díaz, et al., Separation of the sp^3 and sp^2 components in the C1s photoemission spectra of amorphous carbon films, Phys. Rev. B 54 (11) (1996) 8064–8069, https://doi.org/10.1103/PhysRevB.54.8064.

[77] Yu.V. Butenko, et al., Photoemission study of onionlike carbons produced by annealing nanodiamonds, Phys. Rev. B 71 (2005) 7, https://doi.org/10.1103/PhysRevB.71.075420.

[78] Yusuke Taki, Osamu Takai, XPS structural characterization of hydrogenated amorphous carbon thin films prepared by shielded arc ion plating, Thin Solid Films 316 (1) (1998) 45–50, https://doi.org/10.1016/S0040-6090(98)00386-1.

[79] Sabrina S. Jedlicka, Jenna L. Rickus, Dmitry Y. Zemlyanov, Surface analysis by X-ray photoelectron spectroscopy of sol-gel silica modified with covalently bound peptides, J. Phys. Chem. B 111 (40) (2007) 11850–11857, https://doi.org/10.1021/jp0744230.

[80] S. Kaciulis, Spectroscopy of carbon: from diamond to nitride films, Surf. Interface Anal. 44 (8) (2012) 1155–1161, https://doi.org/10.1002/sia.4892.

[81] Lucia Calliari, AES and core level photoemission in the study of a-C and a-C:H, Diam. Relat. Mater. 14 (8) (2005) 1232–1240, https://doi.org/10.1016/j.diamond.2004.10.046.

[82] J.E. Houston, et al., Relationship between the Auger line shape and the electronic properties of graphite, Phys. Rev. B 34 (2) (1986) 1215.

[83] J.C. Lascovich, R. Giorgi, S. Scaglione, Evaluation of the sp^2/sp^3 ratio in amorphous carbon structure by XPS and XAES, Appl. Surf. Sci. 47 (1) (1991) 17–21, https://doi.org/10.1016/0169-4332(91)90098-5.

[84] J.C. Lascovich, S. Scaglione, Comparison among XAES, PELS and XPS techniques for evaluation of Sp^2 percentage in a–C:H, Appl. Surf. Sci. 78 (1) (1994) 17–23, https://doi.org/10.1016/0169-4332(94)90026-4.

[85] Stanfield Y. Lee, et al., Ascertaining the carbon hybridization states of synthetic polymers with X-ray induced Auger electron spectroscopy, J. Phys. Chem. C 122 (22) (2018) 11855–11861, https://doi.org/10.1021/acs.jpcc.8b02217.

[86] J.E. Houston, et al., Relationship between the Auger line shape and the electronic properties of graphite, Phys. Rev. B 34 (1986) 1215–1226, https://doi.org/10.1103/PhysRevB.34.1215.

[87] Beata Lesiak, et al., C sp^2/sp^3 hybridisations in carbon nanomaterials – XPS and (X)AES study, Appl. Surf. Sci. 452 (2018) 223–231, https://doi.org/10.1016/j.apsusc.2018.04.269.

[88] Yusuke Mizokawa, et al., Comparison of the CKLL first-derivative auger spectra from XPS and AES using diamond, graphite, SiC and diamond-like-carbon films, Surf. Sci. 182 (3) (1987) 431–438, https://doi.org/10.1016/0039-6028(87)90011-2.

[89] A.A. Galuska, H.H. Madden, R.E. Allred, Electron spectroscopy of graphite, graphite oxide and amorphous carbon, Appl. Surf. Sci. 32 (3) (1988) 253–272, https://doi.org/10.1016/0169-4332(88)90012-8.

[90] J. Zemek, J. Zalman, A. Luches, XAES and XPS study of amorphous carbon nitride layers, Appl. Surf. Sci. 133 (1) (1998) 27–32, https://doi.org/10.1016/S0169-4332(98)00181-0.

[91] E. Desimoni, et al., Activation of carbon fibres by negative d.c. corona discharge at ambient pressure and temperature, J. Electron Spectrosc. Relat. Phenom. 70 (1) (1994) 1–9, https://doi.org/10.1016/0368-2048(94)02207-G.

[92] Abraham Savitzky, Marcel J.E. Golay, Smoothing and differentiation of data by simplified least squares procedures, Anal. Chem. 36 (8) (1964) 1627–1639, https://doi.org/10.1021/ac60214a047.

[93] Iman Faridmehr, et al., Correlation between engineering stress-strain and true stress-strain curve, Am. J. Civ. Eng. Archit. 2 (1) (2014) 53–59, https://doi.org/10.12691/ajcea-2-1-6.

[94] Joseph R. Davis, Tensile Testing, ASM International, ISBN 978-1-62708-355-3, 2004, https://doi.org/10.31399/asm.tb.tt2.9781627083553.